PHYSICAL REVIEW A **76**, 042116 (2007)

Hydrogenic Lamb shift in iron Fe^{25+} and fine-structure Lamb shift

C. T. Chantler*
School of Physics, University of Melbourne, Victoria 3010, Australia

J. M. Laming
Space Science Division, Code 7674L, Naval Research Laboratory, Washington, D.C. 20375, USA

D. D. Dietrich
Lawrence Livermore National Laboratory, California 94550, USA

W. A. Hallett
GSK Clinical Imaging Centre, Imperial College, Hammersmith Hospital, London, United Kingdom

R. McDonald
MS 72-150, Lawrence Berkeley National Laboratory, Berkeley, California 94270, USA

J. D. Silver
University of Oxford, Clarendon Laboratory, Parks Road, Oxford OX1 3PU, United Kingdom

(Received 22 April 2007; revised manuscript received 23 July 2007; published 18 October 2007)

$1s$-$2p$ Lyman α transitions in hydrogenic iron Fe^{25+} have been observed from a beam-foil source in fourth-order diffraction off ADP 101 and PET 002 crystals, simultaneously with the $n=2$ to $n=4$ Balmer β transitions diffracted in first order. Calibration of the local dispersion relation of the spectrometer using Balmer β lines provides measurements of Lyman α wavelengths. The approach of fitting the full two-dimensional dispersion relation, including other members of Balmer and Lyman series, limits random and systematic correlation of parameters, and reveals a major systematic due to dynamical diffraction depth penetration into a curved crystal. The development of a theory of x-ray diffraction from mosaic crystals was necessary for the accurate interpretation of the experimental data. Photographic theory was also developed in the process of this research. Several systematics are discussed and quantified for the first time for these medium-Z QED comparisons. $2s$-$1s$ and $4f$-$2p$ satellites are explicitly investigated, and a dominant systematic is uncovered, which is due to the variable location of spectral emission downstream of the beam-foil target. $1s$-$2p_{3/2}$, $1s$-$2p_{1/2}$ iron Lamb shifts are measured to be $35\,376 \pm 1900\ \mathrm{cm}^{-1}$ and $35\,953 \pm 1800\ \mathrm{cm}^{-1}$. These agree with but lie higher than theory. This represents a 5.7% measurement of the hydrogenic $1s$-$2p_{1/2}$ Lamb shift in iron. The technique also reports the iron $2p_{3/2}$-$2p_{1/2}$ fine structure as $171\,108\ \mathrm{cm}^{-1} \pm 180\ \mathrm{cm}^{-1}$, which represents a 51% measurement of the hydrogenic iron fine-structure Lamb shift, and reports measurements of secondary lines.

DOI: 10.1103/PhysRevA.76.042116 PACS number(s): 12.20.Fv, 31.30.Jv, 32.30.Rj, 34.80.Kw

I. INTRODUCTION

Numerous tests of quantum electrodynamics (QED) have excited the imagination and interest of researchers since Lamb and Retherford [1]. Tests of exotic atoms and few-electron systems have provided the most critical and successful tests of current theory [2–4]. Impressive precision of low-Z measurements has led to investigations of nuclear form factors and polarization, which involve interesting physics in their own right [5,6]. Strong development has also proceeded in the regime of "highest" coupling strength $(Z\alpha)\rightarrow 1$ for uranium, in particular [7,8]. Meanwhile, medium-Z techniques have been developed over the last two decades, with a view to probing QED in the regime of high effective coupling strength [9–11]. Motivation arises from the increasing significance of higher-order QED terms, together with the $(Z\alpha)^4$ dependence of the lowest-order QED contributions, depending upon the formalism used for the theoretical expansions [12,13]. These QED contributions are here defined to be those not following from relativistic Dirac theory, but to include the self-energy, vacuum polarization, and other specifically QED terms [14]. The dependence upon $Z\alpha$ indicates another strong motivation for these investigations, namely, that as $Z\alpha$ approaches unity for high-Z elements, the convergence of higher-order terms may fail, and additional interactions may, in principle, be observed.

This paper presents data taken at the Lawrence Berkeley Laboratory, Berkeley, California, on the SuperHilac linear accelerator. Results are presented for hydrogenic spectra of iron Fe^{25+}, and in particular, for the Lyman α transitions $1s$-$2p_{3/2}$ and $1s$-$2p_{1/2}$. Measurements in medium-Z hydrogenic systems have used a variety of accelerators and plasma sources. Beam-foil spectroscopy can avoid much of the usual satellite contamination if appropriate stripping and excitation requirements are followed. In particular, the preparation of a beam of bare Fe^{26+} followed by the interaction with a thin $(9-50\ \mu\mathrm{g\ cm}^{-2})$ carbon foil produces a single-interaction regime and a single capture-excitation process predominantly,

---

*chantler@physics.unimelb.edu.au

and is the cleanest excitation condition for precision accelerator-based spectroscopy [9]. Of course, electron beam ion trap (EBIT) plasmas can also provide satellite-free spectra under appropriate conditions [15].

This x-ray regime invites the use of Bragg diffracting crystals for collecting photons from deexcitation processes and for providing the spectral resolution necessary for precision calibrations. This paper uses the dual-arm Johann curved crystal spectrometer designed and constructed at Lawrence Livermore National Laboratory and denoted SS1 [16,17].

Considerable design and analysis effort has addressed potential Doppler shifts and other systematic corrections. In particular, the Lyman α–Balmer β comparison method has been used to isolate systematics due to fast spectral shifts compared to stationary (laboratory-frame) reference sources [9,18]. The validity and applicability of this approach is discussed below. Analysis of the data has involved the development of theoretical tools to evaluate and constrain systematics which have been allowed for, in these experiments, for the first time.

II. OVERVIEW

This paper presents the experimental configuration and details in Sec. III. Reference is made to other works to simplify the ensuing discussion. Lyman α–Balmer β in-beam comparison for wavelength studies is discussed in a companion paper, which concentrates on observed spectral lines and population models [19]. That paper discusses the development of x-ray diffraction theory from mosaic crystals, which was necessary for the accurate interpretation of the experimental data, and the development of photographic theory necessary to linearize the raw data. This experiment developed methods of curvature of the crystals, which are explained in Sec. IV, concluding the experimental section of this paper.

Theoretical wavelengths are required for spectrometer dispersion and calibration, intensity component and population modeling, and for investigation of the Lamb shift. These are discussed in Sec. V, together with the basic equations of analysis of the experimental data.

The fitting of experimental data and determination of the single interaction regime is discussed in the companion paper, together with issues relating to normalization and satellites. This paper briefly summarizes these issues in order to explain the basis of the technique "beyond the Lyman α–Balmer β intercomparison" in Sec. VI. This paper particularly addresses systematics concerning the diffraction process and the spectrometer dispersion function, and so discusses crystal perfection and polarization in Sec. VII, particularly investigating crystal mosaicity and refractive index depth penetration systematic corrections. We present the scales between the (abstract) diffraction theory and the explicit measured positions in microns around the film.

Cascade contributions in such a dilute fast-beam plasma are poorly understood and this experiment has revealed many details about these processes. This is the primary topic of the companion paper and we summarize conclusions briefly in Sec. VIII. This allows us to investigate systematics relating to satellite contamination of all sorts, crystal and diffraction effects intrinsic to curved crystal diffraction, and Doppler shifts relating to differences in decay location of specific states of interest, leading to tabulated results in Sec. IX.

In this context, the approach of fitting the full two-dimensional dispersion relation, including other members of Balmer and Lyman series, significantly limits random and systematic correlation of parameters, and reveals major systematics due to dynamical diffraction depth penetration into a curved crystal and to the decay location. We then observe the fine-structure separation is determined to high accuracy by the current methods, and use this to measure the fine-structure QED contributions and compare this with theory in Sec. X.

In the process we have observed and therefore measured secondary wavelengths, primarily of those satellite or resonance heliumlike transitions, which could have affected the primary measurements of Lyman α and Balmer β components. We therefore present these in Sec. XI. Due to statistics, these are not of high accuracy, but they are clean and useful. Finally, we summarize the conclusions of this paper (Sec. XII).

III. EXPERIMENT

A 500 μg cm^{-2} carbon stripper foil was used to produce an equilibrium distribution of charge states. Of this distribution, a 400 nA average of bare Fe^{26+} (or about 2% of the total) is selected with a bending magnet for delivery to the target. The energies used were 8.3 MeV/amu or approximately 480 MeV, $\beta \simeq 0.1335$, with a series of exposures of from 1.3 mC to 11.9 mC on a carbon foil target of 5, 9, 25, 50, or 223 μg cm^{-2}. These variations help to confirm the assumption that the thin foils corresponded to a single capture and excitation process. A series of multiple collisions and electron capture-ionization processes would decelerate the beam and produce predominantly heliumlike and lithiumlike spectra. This satellite contamination has been a significant problem in other experiments, but is conclusively ruled out by observed spectra. More details are given in a companion paper [19], but Fig. 1 presents the key details for alignment. The beam coming out of the page interacts with the thin carbon foil B producing x rays, which diffract off one of two diffracting crystals on opposite sides of the target, then being imaged on photographic emulsions on the relevant Rowland circle for that crystal.

IV. CRYSTAL CURVATURE

A major difference between this and previous alignment procedures is the method of bending the crystal and testing crystal curvature. The crystals used for this experiment were all bent at specific points and lines to create cylindrical curvature. Benders used in these experiments were of three types: the two-point and two-bar, eight-point and four-bar, and four-point and two-bar methods. The crystal is pushed from behind against two cylindrical bars aligned parallel to

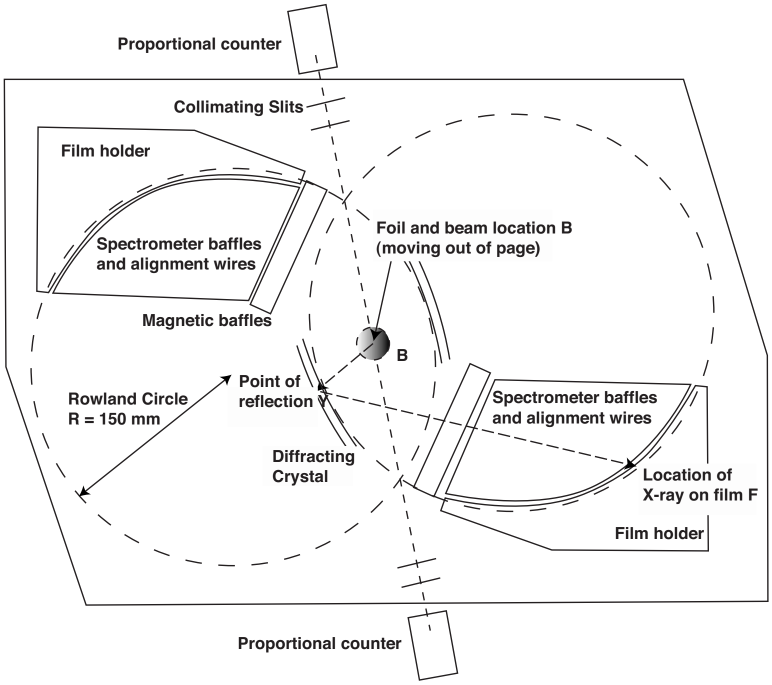

FIG. 1. Layout of the LLNL SS1 spectrometer baseplate. The crystals are arranged to allow two simultaneous Rowland circles with the normalizing proportional counters upstream and downstream and the photographic film aligned mechanically to lie on the Rowland circle to high accuracy. Magnetic baffles suppress stray electrons from reaching the emulsion. The axis of the ion beam (B), the "point of reflection" inside the crystal (Y), and the point of absorption on the photographic film (F) are labeled.

one another and normal to the base. The pushing is achieved by two or four fine-threaded screws with ball bearings at the front to avoid scratching or pulling the rear surface of the crystal. Pushers are located outside the bars, and if the rectangular crystal is of the appropriate size and aligned correctly, the region between the bars forms a near-perfect cylinder of constant radius [20,21].

The two-point method is inferior and gives a small concave distortion in the vertical direction away from the plane in which the points lie. The four-point method is near perfect if the separation of the points is between $\frac{1}{3}$ and $\frac{1}{2}$ of the crystal height and the crystal is centered correctly. An improved alternative is the four-bar method, which can minimize distortion if all bars are exactly parallel to the crystal axis. More recent developments are discussed elsewhere [22], especially including high-accuracy curvature methods for triangular crystals [10]. The front bars are typically 40 mm apart.

Initial bending proceeds until the crystal is seen to focus a parallel diffraction-broadened laser source at an approximately correct distance. A precision $2R=300$ mm mirror is set up in an equivalent mount to allow comparison. A 45° beam splitter is aligned to be precisely parallel to this source and reflection. The mirror and mount are placed in a second location, and the stage adjusted so that the same mirror and mount geometry (defined by the Rowland circle on the spectrometer baseplate) focus to the same location. A second standard mirror may then be placed in the other position to observe a null interference pattern between the two. Test crystals replace this second mirror, and the bending and adjustment proceeds until the interference pattern is minimized.

Crystals are left in their individual mounts for the duration of the experiment. Soft crystals [such as Penta-Erythritol (PET) 002] deform plastically and should be checked regularly and used as soon as possible after bending. The relaxation becomes significant over a few days, and they should be realigned before an exposure if this period has elapsed. ADP 101 deforms slowly over a period of months (for our radii of curvature) so this is not significant. PET crystals were realigned before the experiment, and ADP crystals were checked to show this unnecessary. Realignment implies that mosaic character has been introduced to the curved PET crystals. The results of focusing for a given crystal may be given by the active height and length of the focused or observed region and the fringes of 6348 Å HeNe light along each direction. Typical curvature radii were $2R=300.06$ mm ± 0.03 mm, constant over most of the central diffracting area of the crystal.

Crystal faces were also set perpendicular to the baseplate by comparison to an optical flat (flat and parallel to $\frac{\lambda}{4} \simeq 1500$ Å) with an autocollimator. These are optical tests, and crystal planes are not necessarily parallel to the front surfaces, but any difference was observed to be small from x-ray source calibration tests.

V. THEORETICAL INPUT, DOPPLER SHIFTS, AND ANALYTIC DEVELOPMENT

For $n=1$ and $n=2$ levels, the source of theoretical wavelengths for comparison to experiment is straightforward, given the agreement between results for the two most comprehensive computations [23,24]. However, this is not true for the higher-n levels and hence the Balmer transition energies. Values of Erickson [25] must be corrected for improved values of constants, Dirac energies, and QED terms [20] (particularly the Bethe logarithms [26]). Estimated theoretical uncertainties in the resulting wavelengths lie at the few parts per million (ppm) level. Heliumlike resonance transitions can be observed, and values for these states follow Drake [27] and Vainshtein [28], with corrections of the latter following Drake for higher-n levels [20]. Because of these

TABLE I. Theoretical wavelengths and uncertainties used for important components (no Doppler or refractive index shifts included in this table). On good plates most of these peaks were identifiable, with some of the fine structure unresolved. Energy levels for hydrogenic Fe $1s, 2s, 2p_{1/2}, 2p_{3/2}$ following [23,24]; higher-n levels for hydrogenic Fe corrected from [25] following [20,26]; heliumlike transitions for $n=1,2$ states following [27]; higher-n levels corrected from [28] following [20].

(a) Diffraction in third through fifth order	
$^{26}\mathrm{Fe}^{56}$	Identification
1.3640227±25 Å	Ly ζ $1s_{1/2}$-$7p_{3/2}$
1.3640892±5 Å	Ly ζ $1s_{1/2}$-$7p_{1/2}$
1.3743005±25 Å	Ly ε $1s_{1/2}$-$6p_{3/2}$
1.3744198±5 Å	Ly ε $1s_{1/2}$-$6p_{1/2}$
1.3916957±5 Å	Ly δ $1s_{1/2}$-$5p_{3/2}$
1.3919076±5 Å	Ly δ $1s_{1/2}$-$5p_{1/2}$
1.4249049±5 Å	Ly γ $1s_{1/2}$-$4p_{3/2}$
1.4253392±5 Å	Ly γ $1s_{1/2}$-$4p_{1/2}$
1.5023505±6 Å	Ly β $1s_{1/2}$-$3p_{3/2}$
1.5034963±6 Å	Ly β $1s_{1/2}$-$3p_{1/2}$
1.5731742±14 Å	$1s2\ {}^1\mathrm{S}^0$-$1s3p\ {}^1\mathrm{P}^1$
1.5741512±14 Å	$1s2\ {}^1\mathrm{S}^0$-$1s3p\ {}^3\mathrm{P}^2$
1.5750330±14 Å	$1s2\ {}^1\mathrm{S}^0$-$1s3p\ {}^3\mathrm{P}^1$
1.7780163±6 Å	Ly $\alpha 1s_{1/2}$-$2p_{3/2}$
1.7833157 Å	$1s_{1/2}$-$2s_{1/2}$
1.7834420±6 Å	Ly α $1s_{1/2}$-$2p_{1/2}$
1.8503984±16 Å	$1s2\ {}^1\mathrm{S}^0$-$1s2p\ {}^1\mathrm{P}^1$
1.8554114±16 Å	$1s2\ {}^1\mathrm{S}^0$-$1s2p\ {}^3\mathrm{P}^2$
1.8595157±16 Å	$1s2\ {}^1\mathrm{S}^0$-$1s2p\ {}^3\mathrm{P}^1$
(b) Diffraction in first order	
5.5508548±120 Å	Ba 8 $2p_{1/2}$-$10d_{3/2}$
5.6039402±120 Å	Ba 8 $2p_{3/2}$-$10d_{5/2}$
5.6051160±120 Å	Ba 7 $2p_{1/2}$-$9d_{3/2}$
5.6056865±75 Å	Ba 7 $2p_{1/2}$-$9s_{1/2}$: weak
5.6065446±120 Å	Ba 7 $2s_{1/2}$-$9p_{3/2}$: weak
5.6071319±75 Å	Ba7 $2s_{1/2}$-$9p_{1/2}$: weak
5.6591961±120 Å	Ba 7 $2p_{3/2}$-$9d_{5/2}$: weak
5.6593928±120 Å	Ba 7 $2p_{3/2}$-$9d_{3/2}$: weak
5.6599744±75 Å	Ba 7 $2p_{3/2}$-$9s_{1/2}$: weak
5.6827923±120 Å	Ba ζ $2p_{1/2}$-$8d_{3/2}$: weak
5.6836276±80 Å	Ba ζ $2p_{1/2}$-$8s_{1/2}$: weak
5.6842608±120 Å	Ba ζ $2s_{1/2}$-$8p_{3/2}$: weak
5.6851208±80 Å	Ba ζ $2s_{1/2}$-$8p_{1/2}$: weak
5.7383033±120 Å	Ba ζ $2p_{3/2}$-$8d_{5/2}$
5.7385914±120 Å	Ba ζ $2p_{3/2}$-$8d_{3/2}$: weak
5.7394432±80 Å	Ba ζ $2p_{3/2}$-$8s_{1/2}$: weak
5.8000551±124 Å	Ba ε $2p_{1/2}$-$7d_{3/2}$
5.8013548±86 Å	Ba ε $2p_{1/2}$-$7s_{1/2}$: weak
5.8015848±124 Å	Ba ε $2s_{1/2}$-$7p_{3/2}$: weak
5.8029228±86 Å	Ba ε $2s_{1/2}$-$7p_{1/2}$: weak
5.8577442±124 Å	Ba ε $2p_{3/2}$-$7d_{5/2}$
5.8581925±124 Å	Ba ε $2p_{3/2}$-$7d_{3/2}$: weak
5.8595184±86 Å	Baε $2p_{3/2}$-$7s_{1/2}$: weak
5.9905568±130 Å	Ba δ $2p_{1/2}$-$6d_{3/2}$: weak
5.9921887±130 Å	Ba δ $2s_{1/2}$-$6p_{3/2}$: weak
5.9927597±90 Å	Ba δ $2p_{1/2}$-$6s_{1/2}$: weak
5.9944567±90 Å	Ba δ $2s_{1/2}$-$6p_{1/2}$: weak
6.0518363±130 Å	Ba δ $2p_{3/2}$-$6d_{5/2}$
6.0525964±130 Å	Ba δ $2p_{3/2}$-$6d_{3/2}$: weak
6.0548452±92 Å	Ba δ $2p_{3/2}$-$6s_{1/2}$: weak
6.3357635±100 Å	Ba γ $2p_{1/2}$-$5d_{3/2}$
6.3375806±100 Å	Ba γ $2s_{1/2}$-$5p_{3/2}$: weak
6.3400260±101 Å	Ba γ $2p_{1/2}$-$5s_{1/2}$:weak
6.3419777±101 Å	Ba γ $2s_{1/2}$-$5p_{1/2}$: weak
6.4037265±103 Å	Ba γ $2p_{3/2}$-$5d_{5/2}$
6.4052007±103 Å	Ba γ $2p_{3/2}$-$5d_{3/2}$: weak
6.4095571±103 Å	Ba γ $2p_{3/2}$-$5s_{1/2}$: weak
6.7026528±260 Å	$1s2s\ {}^3\mathrm{S}_1$-$1s5p\ {}^3P_2$
6.8133011±260 Å	$1s2p\ {}^3P_1$-$1s5d\ {}^3D_2$
6.8145487±260 Å	$1s2s\ {}^1S_0$-$1s5p\ {}^1P_1$
6.8196756±260 Å	$1s2p\ {}^3P_0$-$1s5s\ {}^3S_1$
6.8675974±260 Å	$1s2p\ {}^3P_2$-$1s5d\ {}^3D_3$
6.9369294±260 Å	$1s2p\ {}^1P_1$-$1s5d\ {}^1D_2$
6.9460845±260 Å	$1s2p\ {}^1P_1$-$1s5s\ {}^1S_0$
7.0878076±126 Å	Ba β $2p_{1/2}$-$4d_{3/2}$
7.0900726±126 Å	Baβ $2s_{1/2}$-$4p_{3/2}$
7.0982442±126 Å	Ba β $2p_{1/2}$-$4s_{1/2}$
7.1005354±126 Å	Ba β $2s_{1/2}$-$4p_{1/2}$
7.1712089±129 Å	Ba β $2p_{3/2}$-$4d_{5/2}$
7.1748204±129 Å	Ba β $2p_{3/2}$-$4d_{3/2}$
7.1855150±129 Å	Ba β $2p_{3/2}$-$4s_{1/2}$
7.4826961±8735 Å	$1s2s\ {}^3S_1$-$1s4p\ {}^3P_2$
7.6167420±8000 Å	$1s2p\ {}^3P_1$-$1s4d\ {}^3\mathrm{D}_2$
7.6177208±3920 Å	$1s2s\ {}^1S_0$-$1s4p\ {}^1P_1$
7.6414310±8400 Å	$1s2p\ {}^3P_0$-$1s4s\ {}^3S_1$
7.6830272±8000 Å	$1s2p\ {}^3P_2$-$1s4d\ {}^3D_3$
7.7696455±8000 Å	$1s2p\ {}^1P_1$-$1s4d\ {}^1D_2$
7.7920459±1680 Å	$1s2p\ {}^1P_1$-$1s4s\ {}^1S_0$
9.5320492±275 Å	Ba α $2p_{1/2}$-$3d_{3/2}$

corrections, a detailed summary of relevant theoretical transition energies is given in Table I.

The issues of Doppler shifts and broadening provide critical uncertainties in beam-foil spectroscopy. The double-crystal setup of the SS1 provides information on these shifts from comparison of the spectra from each detector. Any nonzero beam angle to the spectrometer will shift wavelengths from one circle up and the other down by an equal amount, and the average of these results is then independent of the first-order shift. This may be used to derive the beam angle if

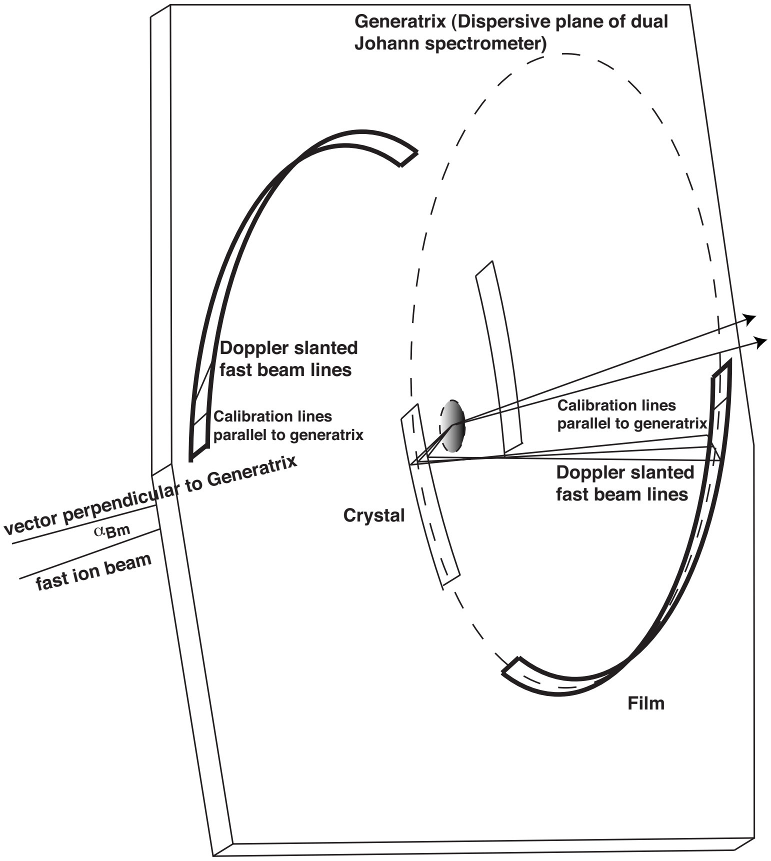

FIG. 2. SS1 spectrometer, showing the origin of Doppler-slanted lines. α_{Bm} is the angle of the incident beam with respect to the crystal generatrix.

both circles are equally well focused. However, this could be subject to differences due to the bending or perfection of individual crystals.

The use of photographic or other two-dimensional detection also provides the value of β via the slope of curved fast-beam lines (Fig. 2). This perspective view of Fig. 1 illustrates that spectral lines from a stationary source will be flat or horizontal, while spectral lines from the target source will be slanted by the Doppler velocity, and the data can therefore accurately characterize both the angle of the detector plane to the beam and the Doppler velocity itself. Figure 3 gives the perspective perpendicular to the detector plane to illustrate the diffraction path to the crystal point X, to the mean penetration depth of the wave field inside the crystal Y, and to the film F, thus defining the angle α_1. In the rest frame of the beam, and inside the diffracting crystal, the relation of wavelength to Bragg angle is straightforward as follows:

$$n\lambda = 2d \sin \theta. \tag{1}$$

Doppler shifts and broadening provide critical uncertainties in beam-foil spectroscopy. The double-crystal setup of the SS1 provides information on these shifts from comparison of the spectra from each detector. Any nonzero beam angle to the spectrometer will shift wavelengths from one circle up and the other down by an equal amount, and the average of these results is then independent of the first-order shift. This may be used to derive the beam angle if both circles are equally well focused. However, this could be subject to differences due to the bending or perfection of individual crystals.

However, the relativistic transformation complicates this, refractive index shifts correct the equation for x rays incident from a vacuum, any off-axis radiation will have a different angle of intersection with the crystal (for the same $[X]$ position on the film), and other defocusing and alignment considerations are important. Details of the fitting formulas and consequent assumptions are relegated to Ref. [20], but the basic diffraction relation for a fast-beam line may be given as

$$\lambda_{inc} = \lambda_{th} \frac{[1 - \beta \sin(\alpha_1 + \alpha_{beam})]}{\sqrt{1 - \beta^2}} \tag{2}$$

$$= \frac{2d}{n}\left(1 - \frac{4d^2}{n^2}\frac{\delta}{\lambda_{inc}^2}\right) \sin \theta_1 \cos \alpha_1. \tag{3}$$

This involves the rest frame wavelength λ_{th} and the value on the film and crystal λ_{inc} (which varies with the film and crystal location), the lattice spacing of the diffracting planes $2d$, the Doppler velocity $\beta = v/c = 0.1360 \pm 0.0005$, the angle of the beam relative to the beamline and spectrometer $\alpha_{beam} = (0.00 \pm 0.08)$ radians, the order of diffraction n, a correction for the refractive index and possible Johann focusing errors δ, and α_1 is the angle away from the generatrix of the cylindrically bent spectrometer. The projection of the angle of incidence (on the crystal surface) onto the plane of the generatrix is given by θ_1. Knowledge of θ_1 and the beam alignment gives the determined wavelengths. Shifts of centroids $[X]$ relative to some reference $[X_{ref}]$ for each scan along the film may then be given by the absolute arclength

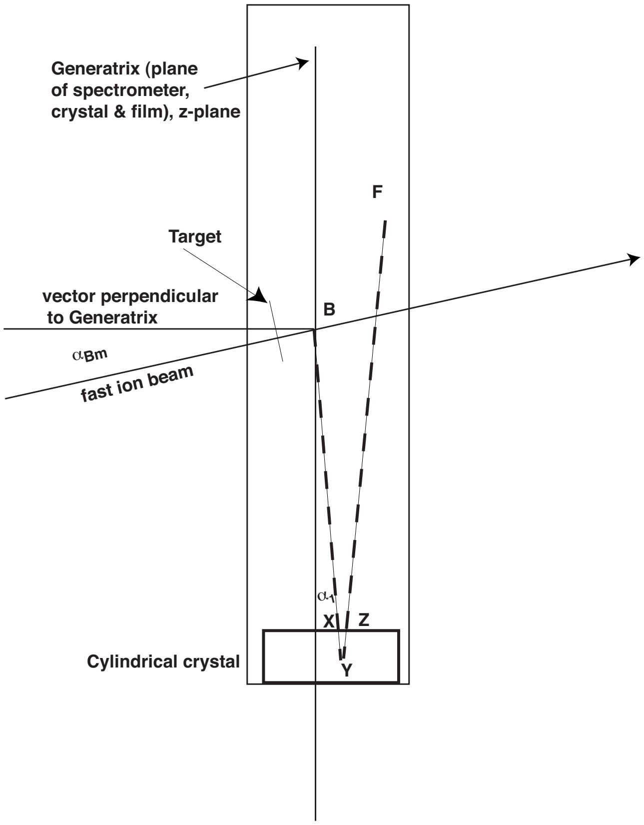

FIG. 3. SS1 spectrometer, side on, showing the x-ray path into and out of the crystal (assuming particlelike ray tracing). α_{Bm} is the angle of the incident beam with respect to the crystal generatrix. α_1 is the angle of the x-ray path away from the generatrix, to the film location.

around the Rowland circle, along the generatrix, from an unknown Y_{ix} to the reference Y_{ref}.

This scaling is affected by the accuracy of the alignment of the densitometer measuring the photographic emulsion, yielding a correction by cos α' cos α'' (Fig. 4). The first term relates to misalignment of the densitometer measurement axis with the generatrix $\alpha' = (0.052 \pm 0.015)$ rad, and the second relates to misalignment of the scanning drive axis $\alpha'' = (0.00 \pm 0.01)$ rad. Inequivalence between lateral and longitudinal densitometry drive steps is allowed for via a parameter $N_1 = 1.00 \pm 0.02$ (see Fig. 4). Other parameters are the crystal curvature $2Rz = (300.00 \pm 0.05)$ mm, the distance from the center of the source to the crystal center $BXz = (26.0 \pm 1.0)$ mm, the distance from the center of the source to the Rowland circle $BDz = (15.0 \pm 1.0)$ mm, and the distance of the foil plane behind the central plane of the film and spectrometer $w_0 = (0.0 \pm 2.0)$ mm. Mechanical alignment constrains these parameters within the ranges indicated, but fitting procedures can reduce uncertainty. These parameters quantify the independent variables and relate film location to the angle θ_1. Uncertainties due to the geometry have small effects on resulting film centroids.

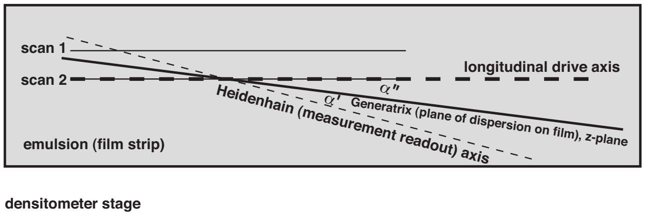

FIG. 4. Variable fitted, which are associated with the densitometry, i.e., with the measurement of the two-dimensional curves on the photographic emulsions. The densitometer stage has a Heidenhain axis, not necessarily coincident with the stepping motor drive axis, so the angle between the two is $\alpha' + \alpha''$ (exaggerated). The angle between the drive axis and the intersection of the generatrix with the film is α''. The transverse drive (although not a dominant variable) may also have a different gear ratio to the longitudinal drive, or may not be at exactly 90°. Most of these parameters were tested to be explicitly negligible.

Curved fast beam lines quantify the Doppler shifts, *subject to* correct identification of the generatrix of the crystal and the zero of the spectrometer plane w_0 (for comparison to static calibration lines). *In-beam calibration lines* with the same Doppler shifts as the Lyman lines—rather than static calibration sources, with different source regions and hence uncertain systematics—eliminate much of this difficulty. In measurements of the $1s$-$2p$ Lyman α Lamb shifts, the transitions involved nearly overlap in fourth order with those of 2-4 Balmer β in first order. This near coincidence provides the major in-beam calibration required. Although this would be true for any Z, in medium-Z ions the separation between the components of interest is sufficiently small that the x-ray wavelength of the Lyman-α transition relative to that of the Balmer-β transition may be accurately determined, yet large enough that only moderate resolution is required to separate the transitions. Since the Balmer β transitions are dominated by d-p transitions, they are much less sensitive to the effects of QED than the Lyman α wavelengths, so these lines may be used to calibrate the spectra and extract a measurement of the Lyman α wavelengths and hence of the $1s$-$2p$ Lamb shifts, dominated by the ground state Lamb shift.

The strongest Balmer line (Balmer β_1, $2p_{3/2}$-$4d_{5/2}$) can generally be used as the reference line. Fits of individual spectral regions allow the consistent use of background levels and widths of the two Lyman α peaks and the seven Balmer β components. Common widths were assumed for each Balmer component, and similarly for the two Lyman components. Lorentzian profiles convolved with aperture functions or Voigt profiles were generally required (neither Gaussian nor Lorentzian profiles adequately represent the peak profiles).

Theoretical widths and relative intensities could be convolved with known instrumental broadening and known diffraction profiles to yield the final intensity profile. However, the relative intensities in foil-excited systems are not well understood theoretically or experimentally. Also, the diffraction and defocusing broadening is dominant and is significantly different for Lyman and Balmer peaks, so the assumption of two independent profiles is valid [20,29,30]. Correlation between fitting parameters (intensities, Gaussian component and total widths, centroids and background parameters) is serious when data are not analyzed correctly.

Monte Carlo determinations of the reduced χ^2 over parameter space is the most robust indicator of this effect [20].

VI. SPECTROSCOPIC DATA BEYOND THE LYMAN α–BALMER β COMPARISON METHOD

The Lyman α–Balmer β intercomparison technique is an excellent relative technique for determining accurate spectroscopy, and in particular, $1s$-$2p$ Lamb shifts compared to $2l$-$4l'$ Lamb shifts. It has often been considered that the QED contributions to the latter are negligible and irrelevant. Later in this paper we prove that this is no longer possible, even for the medium-Z regime. The Lyman α–Balmer β method determines the offset and central wavelength extremely well by interpolation, but can provide a relatively weak determination of scale.

Correlation between fitting parameters can be dominated by small shifts of Balmer β component centroids (and corresponding intensities), since the overall scale of separation of the Balmer components is limited. This baseline dispersion can, however, be determined by reference to other in-beam calibration lines such as Balmer γ and Balmer δ peaks. Such peaks are weaker and hence have larger statistical imprecision, but the increase in baseline more than makes up for this limitation. This "beyond the Lyman α–Balmer β" or "full Balmer calibration" technique is a natural development of the Lyman α–Balmer β comparison method, and gives a significant reduction in the uncertainty of the final result.

Hence the scale of the Balmer spectra can be used to define and constrain any centroiding error. Any inconsistency of results due to this correlation can be observed from the variation in relative intensities.

The quality of the data is indicated by Fig. 5. For low exposures, the residuals after the fit are randomly distributed, indicative of an adequate profile shape. The local χ_r^2 for an individual scan was typically 10 for a typical strong exposure as represented in Fig. 5. Uncertainties are reported as $\sigma\sqrt{\chi_r^2}$, where σ is the output (fitted) one standard deviation uncertainty. The matrix of fitted components is illustrated in the level diagram (Fig. 6).

A typical Balmer γ region is plotted in Fig. 7. Lyman β–Balmer δ regions are also processed but are of course weaker. Independently, these ancillary regions provide weak determinations of QED corrections, primarily due to the relatively low exposures and hence, statistical quality. χ_r^2 values are typically 3–6. The wavelength scale on the emulsion and with the spectrometer are determined to very high accuracy by the ancillary in-beam peaks. The accurate determination of centroids on a common scale across this large range of energy and wavelength is unique for precision QED investigations, and allows numerous systematic errors to be properly addressed.

VII. CRYSTAL PERFECTION AND POLARIZATION

Spectral lines involve diffraction in different orders and with different energies, so the refractive index and geometric corrections are not identical, and should be calculated and included (for each line) prior to the overall least-squares fitting of the independent variables [following Eq. (3)].

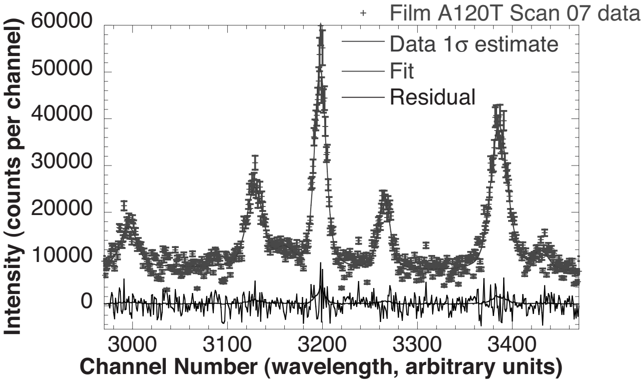

FIG. 5. An individual scan (number 7 of 18) of a particular Rowland circle (A1), emulsion (20), and densitization (0.45 mm height T) using a PET diffracting crystal, for a $9/\mu g\ cm^{-2}$ carbon target thickness, in the region of the Lyman α and Balmer β region of overlap between the first and fourth orders of diffraction. [From left to right, First peak: lines 3 and 4: Ba β $2p_{1/2}$-$4d_{3/2}$, $2s_{1/2}$-$4p_{3/2}$; Second peak: lines 5 and 6: Ba β $2p_{1/2}$-$4s_{1/2}$, $2s_{1/2}$-$4p_{1/2}$; Third peak: 1: Ly α $1s_{1/2}$-$2p_{3/2}$; Fourth peak: 2: Ly α $1s_{1/2}$-$2p_{1/2}$; Fifth peak: lines 7 and 8: Ba β $2p_{3/2}$-$4d_{5/2}$, $2p_{3/2}$-$4d_{3/2}$; Last peak: 9: Ba β $2p_{3/2}$-$4s_{1/2}$]. Lines are labeled in order of increasing wavelength, noting that Lyman transitions have energies approximately 4× that of Balmer transitions and are diffracted in different orders. The residuals are clearly dominated by noise, indicating a consistent fit. Error bars are underestimated by about a factor of 3 as the densitometry signal is dominated by the nonlinearity of the detector response rather than by counting statistics.

Diffraction corrections depend on crystal type and perfection—which can be both a major concern and a convincing test of theory, modeling, and QED. Two major crystal types were used in the experiments: 0.4-mm-thick PET 002 (pentaerythritol) and 0.4-mm-thick ADP 101 (ammonium dihydrogen phosphate) crystals. Intensities and profiles of observed lines with given exposures may be compared to predicted absolute and relative reflectivities of each crystal in first- and fourth-order diffraction. This comparison has proved that flat crystal values are inadequate to explain the results, and that finite curved crystal reflectivities must be used.

The profiles are sensitive to mosaicity and radiation polarization. Observed Lyman and Balmer profiles may be deconvolved to compare instrumental contributions to ideal diffraction and natural linewidths. Equally, ideal linewidths may be convolved with an instrumental profile to compare to experimental results, and to assess profile-dependent centroid correction. Agreement of the resulting profiles was only possible for detected radiation dominated by the strong polarization (E perpendicular to the diffracting plane), for a PET mosaic block width (or *coherence length*) of 0.6 μm, a PET angular (Gaussian) distribution width of less than 0.01 mradians, and an instrumental broadening of approximately 100 μm Lorentzian in profile [30]. ADP results are consistent with negligible mosaicity and hence, near-ideal perfect curved crystal behavior. This is exactly as should be expected, and is a reflection of the different character of

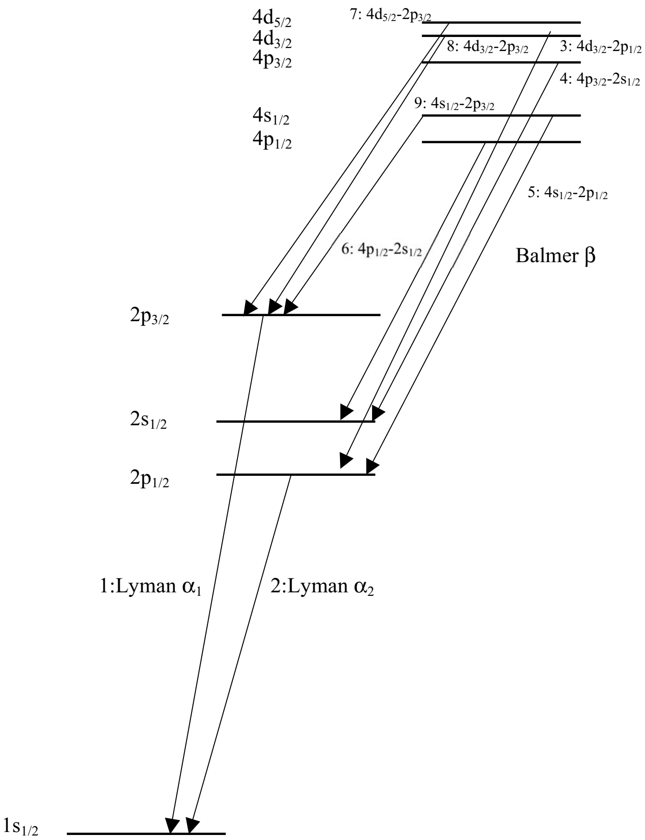

FIG. 6. Dominant electric dipole-allowed hydrogenic transitions in the Lyman α and Balmer β regions, not to scale. Lines are labeled following Fig. 5 in order of increasing wavelength.

these two crystals and the effectiveness of the procedure for producing controlled curvature. The theoretical and experimental profiles are fitted using Voigt functions, and there is a shift due to the profile asymmetry slightly dependent upon the height integrated over in each densitometry scan: $h = 0.45$ mm or $h = 1.00$ mm.

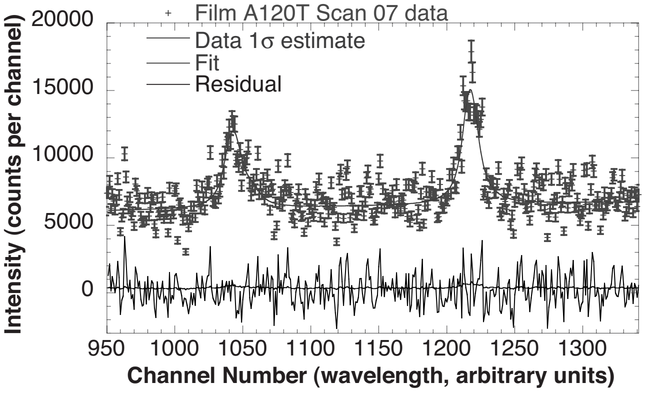

FIG. 7. An individual scan (number 7) of a particular Rowland circle (A1), emulsion (20), and densitization (T) using a PET diffracting crystal, in the region of the Balmer γ region of overlap between the first and fourth orders of diffraction: [Ba γ $2p_{1/2}$-$5d_{3/2}$; Ba γ $2p_{3/2}$-$5d_{5/2}$]. The residuals are clearly dominated by noise, indicating a consistent fit.

The ability to determine these parameters with minimal uncertainty and strong constraints is an excellent demonstration of the diffraction modeling. This theory was the first to address nonideally imperfect crystals using dynamical theory, substantiated by detailed investigations [29,30].

The mosaicity parameters determine and fix the refractive and instrumental centroid corrections, which is the essential prerequisite to fitting the dispersion relation and deriving QED measurements. Tables II and III indicate the diffraction parameters and their uncertainty compared to spectral separations, and the consequent uncertainty in the centroid location. The first table provides measures on the emulsion around the Rowland circle of the spectrometer and detector (in μm); the second table provides a scaling relative to the energy of the primary Lyman α measurement [in parts per million (ppm)].

The conventional refractive index (RI) correction reported in other literature relates to infinite flat crystal diffraction only and is the effective change of angle upon refraction (and hence the apparent change of the spectrometer angle versus wavelength relation). In this experiment the important correction is the systematic shift in measured position between a high-energy Lyman transition x ray (in fourth-order diffraction) and a low-energy Balmer transition x ray (in first-order diffraction), since we are using in-beam calibration in different orders of diffraction to calibrate the spectrometer. The diffractive correction changes in dynamical diffraction from a finite crystal on the Rowland circle compared to the value for an infinite crystal, but in our case this is a minor correction. Geometric corrections for the finite source (instead of a point source) and for the penetration of the x rays into the photographic x ray emulsion are relatively minor.

However, Table II shows that the dynamical diffraction penetration of the x-ray wave field into the diffracting crystal ("before diffracting") is a major correction to this limited picture. It has been extensively discussed [20,29,30]. Perhaps surprisingly, the precision of even "accurate" computations is an important potential systematic for these complex calculations—in other words, convergence and the accuracy of the theoretical prediction should not be ignored. This investigation determined that the mosaicity of the PET crystal was approximately characterized by a block thickness T of around 0.7 μm. The parameter was further refined to 0.6 μm from a comparison of the body of PET data to high precision.

Table II shows that the sensitivity of the diffraction theory to uncertainties in the parameters of the experiment (crystal thickness, beam and crystal angles, and Voigt fitting precisions) are all minor. In other words, the theory and computation are stable and well defined for this experimental geometry and energy.

Systematic shifts of measured Lyman α separations from Balmer β transitions presented in Table II are translated into parts per million of the Lyman energy and into corresponding resolution and energy separation measures for PET crystal data, and for ADP crystal data, in Table III. These corrections are required to determine Lyman α wavelengths, Lamb shift measurements, and fine-structure splittings from the Balmer β calibration spectrum or from the Balmer series calibrations. Relative to the wavelengths, the separation of the strong Balmer components is 11 630 ppm, the Lyman

TABLE II. Theoretical contributions to systematic shifts and theoretical uncertainties in the Lyman α–Balmer β region in Fe^{25+}. Refractive index (RI) corrections in μm to observed (raw) locations on the emulsion, on the Rowland circle. All results give relative shifts for fourth-order diffracting Lyman α radiation compared to those for first-order Balmer β radiation. Variations for other peaks such as Lyman β versus Balmer δ are given elsewhere [20] and effects involving isolated spectral features such as Balmer γ must be computed directly.

Crystal-specific parameters	PET crystal	ADP crystal
RI: Infinite flat perfect crystals	−63.80 μm	−74 μm
RI: (Finite crystal with focusing)	+0.06 μm	
RI: Depth penetration	−97.18 μm	−45 μm
Geometry: Finite source correction	−4.70 μm	
Densitometry: Emulsion penetration	+2.87 μm	+4.74 μm
PET mosaic crystal, 0.7 μm block T[a]		
ADP perfect crystal, medium precision	−148.12 μm	−112.20 μm
Balmer β wavelength ±1.77 ppm	±0.79 μm	±0.49 μm
High precision (0.6 μm PET) shifts	−4.64 μm	+2.90 μm
Contributions to uncertainties due to input parameter uncertainties crystal T[b]	±4.50 μm	±0.02 μm
α_{plane}	±3.93 μm	±1.30 μm
Polarization	−(0.26±0.26) μm	±0E-4 μm
Other (α_{beam})	±0.36 μm	±0.77 μm
Voigt fitting ($h=1.00$ mm)	(+2.95±0.65) μm	(+2.71±0.51) μm
Voigt fitting ($h=0.45$ mm or 0.40 mm)	(+3.74±0.61) μm	(+3.96±0.47) μm
Densitometry	±0.26 μm	±0.26 μm

[a] Block thickness T is the mean size of a mosaic crystallite.
[b] Crystal thickness T is the accuracy of the measured thickness.

fine structure is 3042 ppm, the Lamb shift is expected to be 573.6 ppm, resolution corresponds to approximately 550 ppm, and each 20-μm densitometry step corresponds to 45.4 ppm (PET) or 72.8 ppm (ADP). Compared to these scales, systematic diffraction and geometric shifts for fourth versus first order are dominated by refractive index corrections (primarily for first-order radiation), of 145 ppm (PET) or 269 ppm (ADP), and curved crystal penetration depths (mainly for fourth-order radiation), of 221 ppm (PET) or 164 ppm (ADP). Uncertainty in these corrections is limited *in this experiment* by crystal choice, thickness, and angular tolerance to 13.7 ppm (PET) or 5.86 ppm (ADP). Computational and fitting precision also contribute to these values, which may be compared to the (negligible) theoretical uncer-

TABLE III. Summary of theoretical contributions to systematic shifts and theoretical uncertainties in the Lyman α–Balmer β region in Fe^{25+} in parts per million of the Lyman α x-ray wavelength. Separation of components and (diffraction) systematics.

Balmer f.s. $2p_{1/2}$-$4d_{3/2} \rightarrow 2p_{3/2}$-$4d_{5/2}$	11630 ppm	
Lyman fine structure	3042 ppm	
Lamb shift (theory)	573.6 ppm	
Instrumental resolution	550 ppm	
Crystal-specific parameters	PET crystal	ADP crystal
20-μm-densitometer step	45.4 ppm	72.8 ppm
RI: (Flat crystal) fourth- vs first-order shift	−145±13.7 ppm	−269±5.9 ppm
Curved crystal depth penetration	−221 ppm	−164 ppm
Total high-precision curved crystal shift	−346.8 ppm	−397.9 ppm
Voigt centroid-mean shift ($h=1.00$ mm)	(6.7±1.5) ppm	
Voigt centroid-mean shift ($h=0.45$ mm)	(8.5±1.4) ppm	
Correction for polarization	(−0.59±0.59) ppm	0 ppm

tainty in the Balmer wavelengths used to model the dispersion relation, and to estimated uncertainty in theory of 0.3 ppm. In most cases, experimental uncertainties can be reduced in future experiments without great difficulty.

In assessing convergence and resulting uncertainties of the modeling, all critical parameters have been assessed. For the PET crystal, the mosaic block thickness was an important parameter, and the finite crystal thickness was also significant. Conversely, neither parameter was significant for the experiment involving the ADP crystal. The consistency of both data sets is a strong indicator of the convergence and adequacy of the theoretical determinations of diffractive effects. The fitting of a Voigt profile to a theoretically asymmetric peak yielded a shift for both crystals, and the other most significant contribution to the error budget was the imprecision of α_{plane}, the angle of the Bragg planes to the crystal surface.

VIII. BEAM-FOIL EXCITATION, POPULATIONS, AND SATELLITE CONTAMINATION

In past beam-foil tests of QED (and of other investigations), it has been assumed that prompt or in-target excitation and decay dominated, and any downstream shift was neglected [31]. We call this the C1 component of the decays, which generally increases linearly with thickness in the thin-foil regime. We prove [19] that the thickness-independent component produced at the exit of the foil or downstream is dominant in the thin-foil or near-single-interaction regime (we call this the C2 component). The C1 component might be expected to correspond to multiple excitations or ionizations within the foil. We observe that multiple-electron capture and the relative intensities of dielectronic satellites and related processes increase with thickness, so are indeed dominated by the C1 component.

High-n states cannot decay inside the foil, but $2l$ and $3l$ states do. Dominant noncollisional processes inside the foil are thus $1s$-($1s$-$3l$) hydrogenic capture and deexcitation. This (C1) component may yield nonstatistical Lyman α and β ratios. This component involves exit excitation of (these) hydrogenic states to Yrast states (possibly via convoy electron production), leading to thickness-dependent $4f$-$2p$, $3d$-$1s$, $3d$-$2p$, and $2p$-$1s$ contributions. High-n heliumlike (and lithiumlike) states, neglecting double-capture processes, are primarily produced (in this regime) by capture of electrons by hydrogenic ions, or excitation of heliumlike $1s(1$-$3l)$ states, at the foil exit. These are proportional to target thickness and explain the dependence observed.

The thickness-independent component of hydrogenic spectra is produced by a combination of foil-capture-with-exit-excitation and exit-capture processes. Initial population may involve Stark mixing, but decays are in field-free regions.

The population process is markedly nonstatistical for $n < 5$, and follows complex capture models for the dependence in this region, but is consistent with n^{-3} and statistical populations for $n > 4$, with s-state populations reduced by (40–50)% and with a possible weak peaking for d-f states. This may be due to rapid redistribution, radiative capture of convoy electrons, or other processes. In relation to possible source location shifts, a statistical model (M6 in [19]) is therefore corrected for these lower ($n=2-4$) $2s$, $2p$, $3s$, $3p$, $3d$, and $4s$ initial populations to compare cascade-dependent contributions from medium- and high-n levels.

Lyman radiation appears to be unpolarized, and Balmer β (nd-$2p$) radiation appears significantly π polarized with oscillation along the beam axis. Decay lengths and source locations may be estimated from these models, allowing relevant shifts of Lyman α with respect to Balmer β to be quantified, and allowing estimation of hydrogenic contamination of these peaks. The Yrast contributions are least well defined, and are most amenable to future measurement. Contributions from high-n states are dominated by the Yrast component, by direct population, or by immediate collapse of initial states.

The C1 process contributes minor additional shifts between the determined energies of Lyman and Balmer series spectral peaks, as given in [19]: the decay locations for all thickness-dependent fractions are almost model independent, whether this is due to the wake field or simply to the direct production of excited states within the foil. However, the dominant shift is due to the field-free downstream decay of the observed initial population distribution, and this must therefore be modeled carefully.

IX. BEAM-FOIL DEEXCITATION AND Fe LAMB SHIFTS

Theoretical wavelengths, diffraction and geometric effects, and local fitting results all contribute to the final results. These are presented in the first section of Tables IV and V. Statistical quality lies at the 4–8 ppm level for individual films using either local fits of the Lyman α–Balmer β region at medium or high precision, or using weighted global fits of the whole observed Lyman and Balmer series.

Effects discussed in previous theses and literature (dielectronic heliumlike satellites (1–2 ppm), crystal problems, $2s$-$1s$ and Lyman γ transitions (1–3 ppm), and Stark fields [32,33]) are detailed in [19] but do not contribute significant shifts. Contributions from these sources are quantified in Tables IV and V. New contributions are presented here for satellites due to $4f$-$2p$ decays but are also minor if the location of the decay is at the foil target exit location (3 ppm).

The curved crystal diffraction and focusing model is robust—the results are consistent in detail for both diffracting crystals, which have different contributions from the main two correction factors. The overall theoretical uncertainty of the diffraction modeling (at high precision) varies from 5.8 ppm for ADP crystals to 13.6 ppm for PET crystals. The larger value for PET diffraction is primarily due to the remaining uncertainty in the mosaic block size because PET is neither ideally perfect nor ideally imperfect.

Quoted statistical uncertainties for each film give the unweighted scatter of results. Thicker target results were short exposures due to beam-time constraints, and relatively few scans were densitized, so those statistical uncertainties and scatter are relatively large. The best data from both Rowland circles agree well within one estimated standard deviation. Results from three particular scans [B420 and B415 (for PET

TABLE IV. Hydrogenic iron measurements using the PET diffracting crystal.

Film emulsion	A120T	A120M	B220B	A320A	B420A	A115C	B415A
C target[a]	9	9	9	25	25	50	50
$h(f)$, mm	0.45	1.00	1.00	1.00	1.00	1.00	1.00
Observation length	2 mm	2 mm	1.6 mm	2 mm	1.6 mm	2 mm	1.6 mm
Useful scans[b]	18-6	9-3	9	9	6	9/7-1	7-1
Local Lyα-Baβ fits: Mean, medium precision ppm shift [24], *1 standard deviation statistical uncertainty:*							
Lyman α_1	143.3±6.4	131.7±4.6	139.1±12.2	157.9±9.3	149.2±26.1	142.0±5.8	152.9±19.3
Lyman α_2	143.4±5.6	142.6±6.2	135.0±13.4	143.3±12.6	183.7±20.6	138.6±6.4	168.1±12.4
Weighted global fits of whole Lyman-Balmer series for all scans: Result, medium precision ppm shift [24]:							
Lyman α	149.6±8.6	144.3±3.4	138.8±4.7	152.5±4.9	179.3±8.1	141.8±4.3	165.5±15.5
Total additional correction from high precision results of Table II, *ppm, with* ***theoretical*** *uncertainty*:							
Lyman α_1	2.65±13.8	4.46±13.8	idem	idem	idem	idem	idem
Lyman α_2	2.62±13.6	4.41±13.6	idem	idem	idem	idem	idem
Additional spectral features and transitions, [19], corrections to above, ppm							
Dielectronic satellites							
Lyman α_1	+0.01±1.01	idem	idem	+0.04±2.8	idem	+0.07±5.6	idem
Lyman α_2	+1.93±1.01	idem	idem	+5.4±2.8	idem	+10.8±5.6	idem
Corrections for satellites based upon decay at the foil target exit, ppm:							
$2s$-$1s$+Lyγ, Lyman α_2	−0.91±2.4	idem	idem	idem	idem	idem	idem
$4f$-$2p$decays, Lyman α_1	−3.39±2.0	idem	idem	idem	idem	idem	idem
$4f$-$2p$ decays, Lyman α_2	−3.00±2.0	idem	idem	idem	idem	idem	idem
Fitting errors, corrections to above, ppm							
Fitting error	−19±19	idem	idem	idem	idem	idem	idem
1 Upper limit C2 or thickness-independent source, [19], with 25% increase for $n_{max}>14$							
Correction, Lyman α_1	−29.3±22	idem	idem	idem	idem	idem	idem
Correction, Lyman α_2	−28.9±21	idem	idem	idem	idem	idem	idem
1 Upper limit for fits of each film, PET exposures, [19], ppm							
1 upper limit, ppm, Lyα_1[c]	94.27±6.4	84.48±4.6	91.88±12.2	110.7±9.3	102.0±26.1	94.78±5.8	105.7±19.3
1 upper limit, ppm, Lyα_2[c]	96.12±5.6	97.11±6.2	89.53±13.4	101.3±12.6	141.7±20.6	102.0±6.4	131.5±12.4
1 upper limit, global fits[c]	101.46±8.6	97.96±3.4	92.46±4.7	107.9±4.9	134.7±8.1	99.92±4.3	123.6±15.5
Uncertainty, Lyα_1	±32.9	32.6	34.5	33.7	41.6	33.2	38.0
Uncertainty, Lyα_2	±32.1	32.1	34.3	34.1	37.8	32.7	34.4
2 Lower (Yrast) limit for C2 decay source, [19] (instead of C2 decay estimate above)							
Yrast shift/2 mm	−79±22	idem	idem	idem	idem	idem	idem
2 lower (Yrast) limit, Lyα_1	44.57	34.8	42.18	61.0	52.3	45.08	56.0
2 Lower (Yrast) limit, Lyα_2	46.02	47.0	39.43	51.2	91.6	51.9	81.4

[a] Target thickness, $\mu g\ cm^{-2}$.

[b] Number densitized minus number omitted due to shadowing by alignment wires.

[c] Statistical uncertainty only.

data) and for B417A (for ADP data)] are (therefore) noisy outliers, poor and affected by thickness and B-circle issues discussed earlier. They are therefore omitted from quoted averages. Data suggest a possible additional 6 ppm shift for 50 $\mu g\ cm^{-2}$ targets compared to A120 and B220 (from an overestimate of satellite contributions or a thickness-dependent effect), implying a negligible −1 ppm correction to thin target results.

The normal-incidence dual-arm Johann crystal spectrometer (SS1) and the thin-foil target combine to provide a very localized source of excited ions. The different source position and uncertain population mechanism can yield large sys-

TABLE V. Hydrogenic iron ADP measurements and weighted means.

Film emulsion	A322S	B422S	A317A	B417A[d]	PETav[e]	ADPav[e]	Mean
C target[a]	5	5	9	9			
$h(f)$, mm	0.45	0.45	0.40	0.40			
Observation length	1 mm	1.5 mm	1 mm	1.5 mm			
Useful scans[b]	18-4	16-3	20-2	23-6			
Diffraction modeling and statistical uncertainties, ppm							
Local Lyα-Baβ fits: Mean, Medium precision ppm shift [24], *1 standard deviation statistical uncertainty*:							
Lyman α_1	189.4±13.7	149.8±8.5	191.4±9.3	221.8±10.4			
Lyman α_2	170.6±12.4	157.2±10.0	184.6±7.0	229.8±10.1			
Weighted global fits of whole Lyman-Balmer series for all scans: medium precision ppm shift [24]:							
Lyman α	154.4±14.7	159.4±10.6	194.6±13.8	220.8±10.5			
Total additional correction from high precision results of Table II, *ppm, with theoretical uncertainty*:							
Lyman α_1	−24.64±5.9	idem	−25.05±5.9	idem			
Lyman α_2	−24.47±5.8	idem	−24.97±5.8	idem			
Additional spectral features and transitions, [19], corrections to above, ppm							
Dielectronic satellites, corrections to above, ppm:							
Lyman α_1	−1.09±0.61	idem	−1.96±1.09	idem			
Lyman α_2	−1.01±0.83	idem	−1.81±1.49	idem			
Corrections for satellites based upon decay at the foil target exit, ppm							
$2s$-$1s$+Lyγ, Lyman α_2	−3.0±4.5	idem	idem	idem			
$4f$-$2p$ decays, Lyman α_1	−3.17±2.0	idem	idem	idem			
$4f$-$2p$ decays, Lyman α_2	−2.78±2.0	idem	idem	idem			
Fitting Errors, corrections to above, ppm							
Fitting error	−19±19	idem	idem	idem			
1 upper limit C2 or thickness-independent source, [19], with 25% increase for $n_{max}>14$							
Correction,Lyman α_1	−35.1±35	idem	idem	idem			
Correction, Lyman α_2	−34.4±35	idem	idem	idem			
1 upper limit for fits of each film, ADP exposures and averages, [19], ppm							
1 upper limit, ppm,Lyα_1[c]	106.40±13.7	66.80±8.5	107.12±9.3	137.52±10.4	92.39±7.9	88.84±19.9	91.68±11.4
1 upper limit, ppm, Lyα_2[c]	85.55±12.4	72.2±10.0	98.25±7.0	143.45±10.1	97.87±3.2	88.94±11.2	95.36±7.7
1 upper limit, global fits[c]	70.38±14.7	75.4±10.6	109.3±13.8	135.49±10.5	99.28±4.8	84.63±9.6	98.22±6.5
Uncertainty, Lyα_1	±42.6	41.2	41.4	41.6	33.2	45.0	34.2
Uncertainty, Lyα_2	±42.4	41.8	41.2	41.8	31.7	42.1	32.5
2 lower (Yrast) limit for C2 decay source, [19] (instead of C2 decay estimate above)							
Yrast shift/1mm	−75±35	idem	idem	idem			
2 lower (Yrast) limit,Lyα_1	66.50	26.90	67.22	97.62	42.69	48.94	
2 lower (Yrast) limit, Lyα_2	44.95	31.55	57.65	102.85	47.77	48.34	
3 Yrast estimate based on Lyman β spectra, [19] (additional to C2 decay estimate above)							
Yrast shift					−29.4±23.8	−23.5±19.0	
3 final estimate, local fits, Lyα_1					63.02	65.34	63.54
3 final estimate, local fits, Lyα_2					68.50	65.44	67.64

[a] Target thickness, $\mu g\ \mathrm{cm}^{-2}$.

[b] Number densitized minus number omitted due to shadowing by alignment wires.

[c] Statistical uncertainty only.

[d] After one cycle only.

[e] PET weighted averages over 67-13 scans, omitting poorly determined B420, B415 and ADP average omitting B417 Ly α results.

tematics via relative Doppler shifts at the detector and possible contamination from doubly excited states [18,20,32]. Careful modeling, together with observed values for relative intensities of resolved components, has resulted in the control of this possible error source. Usually this systematic is assumed negligible in in-beam calibration, but it is often too large to be ignored.

Neglecting the decay location leaves a systematic "discrepancy" of 150 ppm. Lyman α wavelengths have longer wavelengths relative to Balmer β than expected. The tables provide three estimates of the correction for the downstream decay location, because this is the largest uncertainty in the analyses.

The first estimate is the "upper limit C2" assuming that any missing intensity is purely due to higher n population ($n_{max}>14$) in a statistical distribution. Individual results from films and densitizations are presented in Table IV for the data from exposures using a PET diffracting crystal, and in Table V for the data from exposures using an ADP diffracting crystal. After all these corrections, the discrepancy is approximately 90 ppm. Individual results can be quoted for specific (local) fits of Lyman α_1 and Lyman α_2, and also for global fits of the full Balmer series. Two uncertainties are listed in the tables: the one standard deviation immediately after the quoted discrepancy is 4–20 ppm, but is dominated by the systematic uncertainty listed in the following two rows of 30–40 ppm.

The overall consistency is remarkable. Uncertainties of the fitting error and the C2 downstream decay prediction are quoted as equal to the magnitudes of the predicted shifts, because of the complexity of these corrections, and because of uncertainty in the partitioning of the Lyman α model-dependent C1 component, C2 direct decay component, simple cascade contribution, and high-n Yrast cascade contributions [19]. The scatter of the derived results is consistent with this final uncertainty, though the weighted statistical uncertainty *per se* suggests that a much smaller uncertainty would be possible in the absence (or full resolution) of these systematics. The weighted means of each set of data are presented in the last three rows of Table V, and show continuing consistency to the level claimed.

Results from PET and ADP diffraction are complementary and limit uncertainties and systematics, giving observed discrepancies for Lyman α_1 and Lyman α_2 wavelengths of $91.68\pm11.4\pm32.3$ ppm and $95.36\pm7.7\pm31.5$ ppm, where the first uncertainty is statistical (one standard deviation) and the second is systematic (Table V, last column). Global fits yield a mean Lyman α discrepancy of $98.22\pm6.5\pm32$ ppm fully consistent with the earlier two estimates. The global fits are particularly helpful for ADP results where each scan has fairly weak Balmer β intensities and the number of scans is large. The global fits include all scans, and find the most self-consistent dispersion with the body of data. They correct the part of the dispersion or fitting error due to the slope, but are subject to offset correction and to satellite discrepancies between Lyman α_1 and α_2. Tabulated final results (using the mean correction for the components) are accurate at the level of these corrections (i.e., ±2 ppm plus the other large uncertainties).

The second estimate provided is the Lower (Yrast) limit assuming Yrast population of $n>4$, $l>3$ states (and mainly $l=n-1$) primarily affecting $2p$-$1s$, $3d$-$1s$, $3d$-$2p$, and $4f$-$2p$ transitions. This population mechanism would yield equal Lyman α and Balmer α intensities, with Lyman β at the 1% level and $4f$-$2d$ transitions at the 0.5% level, all arising from essentially the same source location. This could account for 80% of the iron Lyman α intensity, constrained by widths and relative intensities [19]. This lower limit of the shift (or upper limit to the decay location for Lyman α) is presented in the lower rows of Tables IV and V. This yields an upper limit to the C2 decay location systematic correction. The correction is slightly different for the two crystals, and yields a final estimate of the discrepancy from theory of some 45 ppm with similar uncertainty and consistency as the C2 limit.

Dominant uncertainty (between these two estimates) arises from the Yrast component and the length and position of the observation region. However, this shift and uncertainty is limited by fine structure and Lyman β observations. Lyman β components are not fully resolved, but have (also) been fitted locally with Balmer δ and the dispersion relation. These local measurements are consistent with Lyman β having similar source-dependent corrections and discrepancies as Lyman α. Typical discrepancies of Lyman β and Balmer δ spectra from the global dispersion relation are small, less than 25 μm.

Lyman β appears to lie below the expected level from the global fits. This may be quantified in the PET data to give a mean shift of Lyman β versus α primarily decay location but including diffraction and $3d$-$1s$ effects, which is not dependent on local dispersion or Balmer δ fitting uncertainty. Correction for $3d$-$1s$ is similar to the $4f$-$2p$ correction, so it should not give a relative shift from Balmer β values; $3s$-$1s$ may be ignored; diffraction corrections should be similar; satellites should remain negligible; and the Balmer fitting error is similar.

The best data set (B220B) observes a shift of Lyman β_1 to shorter wavelengths by $27.49\pm10.4\mu$ on the film, or upstream by $202.4\pm76.6\mu$ if all is due to the source location (for further details see [20]). All other data sets are consistent with this, with larger statistical uncertainty. The source location for Lyman β is expected (from decay modeling) to lie 25μ upstream of Balmer radiation, rather than downstream, and this estimate is not strongly dependent on the Yrast contribution. Thus Lyman β radiation is expected to lie 42.7 ppm lower than the global fit, and the difference observed provides a second confirmation of the impact of Yrast decays.

Lyman β results should therefore be reduced by 37.4 ppm. The corresponding correction factor to the final Lyman α Lamb shift discrepancies (due to the same Yrast contributions) is -29.37 ± 23.8 ppm for PET diffraction. ADP diffraction uses a reduced observation length, so the correction should be less than this. The same scaling as the Yrast limit calculation discussed earlier gives an ADP correction of -23.50 ± 19.0 ppm.

This third estimate is then presented for Lyman α_1 and Lyman α_2 wavelengths in the last columns of Table V, carried over for clarity to Table VI. The result lies between the upper C2 and the lower Yrast limits, implying that this final observation and uncertainty agree with the model-dependent

TABLE VI. Differential measurement of iron.

Lyman α and Lyman β wavelengths, and $2p$-$1s$ Lamb shifts				
	PET	ADP	Mean	Mean
Global discrepancy, ppm				
Lyman $\alpha^{a,b}$	69.91[4.8]	61.13[9.6]	69.27[6.5][32.3]	
Local discrepancy, ppm			Lyman α_1	Lyman α_2
Lyman $\alpha_1{}^{b,c}$	63.02[7.9]	65.34[19.9]	63.54[11.4][32.3]	
Lyman $\alpha_2{}^{b,c}$	68.50[3.2]	65.44[11.2]		67.64[7.7][31.5]
Wavelengths, Å, this paper			1.7781293[203][574]	1.7835626[137][562]
Theory, [24], Å			1.7780163[6]	1.7834420[6]
Theory, [25], Å			1.7780439[55]	1.7834690[59]
Lamb shift, cm^{-1}, this paper			35376[641][1817]	35953[432][1766]
Experiment, Silver *et al.* [9], cm^{-1}			36000[6000]	38400[6000]
Experiment, Briand *et al.* [31], cm^{-1}			27400[4800]	33300[5600]
Theory, [24], cm^{-1}			31802[20]	32160[20]
Secondary measurement:			Lyman β_1 $(1s$-$3p_{3/2})$	
Local discrepancy, B220B, ppm			73.30[47.4]	
Global discrepancy, B220B, ppm			55.06[30.3][32.0]	
Wavelengths, Å, this paper			1.5024332[455][481]	
Theory, [19], [24], Å			1.5023505[6]	

[a] Sum over 45 (PET), 71 (ADP) scans.

[b] Statistical followed by systematic uncertainty, ppm discrepancy with respect to [24].

[c] Weighted averages over 67-13 (PET), 77-15 (ADP) scans.

and model-independent limits and uncertainties discussed earlier. They also specifically indicate the magnitude of expected Yrast transitions and confirm their existence. These values remain (correctly) higher than the (43–49)±33 ppm Yrast limit estimates, are physically reasonable and nearly model independent, as opposed to the other two estimates, since they are based on analogous in-beam transitions with similar decay modeling and locations nearly independent of any of the models.

This final result represents a 5.7% measurement of the $1s$-$2p_{1/2}$ Lamb shift (Fig. 8). Dominant uncertainty remains the Yrast contribution, initial populations, and observation region, with possible fitting errors, diffraction corrections, and statistics contributing in order of decreasing significance.

X. $2P_{3/2}$-$2P_{1/2}$ FINE-STRUCTURE MEASUREMENT

Notice that all of the dominant uncertainties are systematic and apply equally to both Lyman α components. Diffraction shifts, source location shifts, and fitting shifts affect both equally. Only minor satellite uncertainties and small uncertainties from asymmetric Balmer shifts contribute to uncertainty of the fine-structure separation. Therefore, it is possible to get high accuracy on a differential measurement of the fine structure separation based on this same data set.

One can derive the fine structure from the final results of Tables IV and V, noting that most of the systematic shifts cancel so that the uncertainties are correlated and do not contribute to this measurement. This result is given in the first row in Table VII, but includes (unnecessary) uncertainty from correlated scatter due to the Balmer fits and B-circle Lyman α_1 contributions; a (much) better estimate is provided from the second row by the individual peak uncertainties and omitting the two poor data sets (B420 and B415).

The resulting fine-structure measurement from PET and ADP data is given in Table VII and Fig. 9. In all cases, separation of the two Lyman α components is remarkably

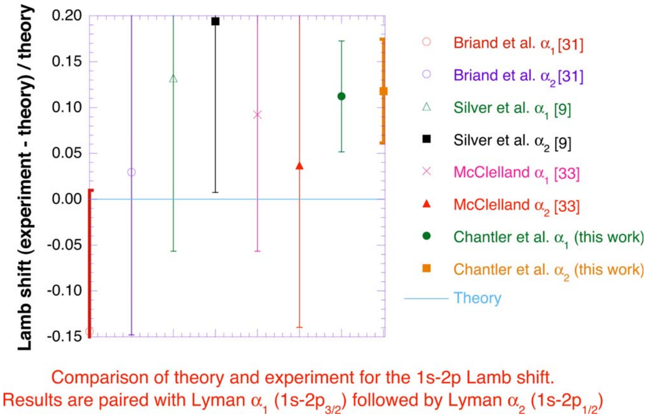

FIG. 8. (Color online) Plot of recent measurements of the hydrogenic Lyman α Lamb shifts for iron. References from Table VI: Briand *et al.* [31]; Silver *et al.* [9]; McClelland [33]; Theory (Johnson and Soff [24]). References given on right correspond to data appearing left to right in figure.

TABLE VII. Measurement of iron $2p_{3/2}$-$2p_{1/2}$ fine structure.

Correction (ppm of Lyman α wavelength)	PET	ADP	Mean
Following Tables IV and V[a]	5.48±8.1 ppm	0.29±35	4.44±20
From text[b]	0.174±3.36 ppm	−0.281±6.0	−0.089±3.0
Weighted mean of PET and ADP sums:			0.0654±0.194 ppm
Residual systematics (ppm of Lyman α wavelength):	PET	ADP	Mean
Diffraction uncertainty:	±0.20 ppm	±0.20 ppm	
Dielectronic satellites[c]:	±1.01 ppm	±1.49 ppm	
$2s$-$1s$+Lyγ:	±2.4 ppm	±4.5 ppm	
$4f$-$2p$ decays:	±0.40 ppm	±0.40 ppm	
Fitting error:	±1.82 ppm	±1.82 ppm	
Decay source:	±0.4 ppm	±0.7 ppm	
Fine structure, ppm of Lyman α wavelength	0.174±4.66 ppm	−0.281±7.90 ppm	0.0654±3.2 ppm
Fine structure, this work, ppm of f.s. interval[b]	57.0[1101][1058]	−92.1[1966][1684]	21.4[63.6][1058]
Δ(cm^{-1}), experiment-theory, this work[d]	9.76±261	−15.76±442	+3.67±181
Δ(cm^{-1}), previous measurement [33][d]			−1804±7400
Δ(cm^{-1}), previous measurement [9][d]			+1896±5300
Δ(cm^{-1}), previous measurement [34][d]			+5650±3228
Δ(cm^{-1}), previous measurement [35][d]			−904±1600
Δ(cm^{-1}), previous measurement [16][d]			+2296±3200
Theory [24]	171104±1 cm^{-1}=±5.8 ppm f.s.		
Theory [25]	171080±30 cm^{-1}=±175 ppm f.s.		
Lamb shift contribution [24]	358±0.99 cm^{-1}=2092±5.8 ppm f.s.		
Lamb shift, this paper, with respect to [24]	1%±51%		

[a] Weighted averages over 67-13 (PET), 77-15 (ADP) scans, omitting B420 and B415 Ly α_2 results.

[b] Sum over 45 (PET), 71 (ADP) scans, including satellite corrections, omitting B420 and B415 (statistical uncertainty only).

[c] Uncertainty for 9 $\mu g\,cm^{-2}$ target results.

[d] Δ is the shift of experiment from the theory of [24].

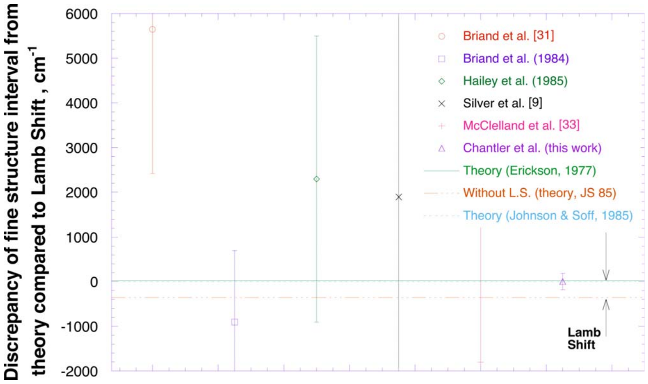

FIG. 9. (Color online) Plot of recent measurements of the hydrogenic fine-structure Lamb shifts for iron. References from Table VII: Briand *et al.* [34]; Silver *et al.* [9]; McClelland [33]; Briand *et al.* [35]; Hailey *et al.* [16]; theory (Johnson and Soff [24]). References given on right correspond to data appearing left to right in figure.

consistent with theory within small statistical and systematic uncertainty.

Improvement over previous beam-foil measurements is dramatic. This appears to be the best measurement in any beam-foil (or Tokamak) system by a factor of 7 [36,37] and is in good agreement with theory. Other recent measurements in this regime [38] are interesting but use quite different methods. This measurement is dominated by statistics, both in the scatter of discrepancy and in the limit to Balmer fitting errors. Agreement between crystals suggests that the earlier $2s$-$1s$ uncertainty was overestimated. Although much less precise than quenching and radio-frequency measurements on hydrogen and helium, the sources of limitation suggest that considerable further improvement may be made.

Corresponding fine-structure measurement in heliumlike systems appears to be sensitive to or approaching sensitivity to $2p$ state QED contributions in $1s2p$ systems (e.g., [10,39–45]), subject to possible $1s$ or $2s$ contribution errors and electron correlation uncertainties, and after correction for significant contributions [46–49]. Some of these issues and advances have been discussed recently [50,51]. Direct measurement of heliumlike $1s2p\ {}^3P_1$-$1s2p\ {}^3P_2$ by laser-induced M6 resonance has quoted a measurement of the fine-structure

TABLE VIII. Iron heliumlike and lithiumlike wavelengths, Å.

Line	Theory	A322S	B422S	A317A	A120M	B220B	A320A	A120T	BX11A
U	6.10000	6.13460(30)[a]		6.12070(120)					
$4\times 1s3p\,^1P_1\text{-}1s^2$	6.29270(0.6)			6.29306(27)					
$1s5p\ ^3P_2\text{-}1s2s\ ^3S_1$	6.70265(3)				6.70081(53)				6.70072(15)
[b]	6.81330(3)				6.81250(53)	6.81140(47)			6.81109(12)
$1s5d\ ^3D_3\text{-}1s2p\ ^3P_2$	6.86760(3)				6.86680(53)	6.86732(49)			6.86613(7.2)
$1s5d\ ^1D_2\text{-}1s2p\ ^1P_1$	6.93693(3)								6.93577(13)
$4\times 1s2p\ ^1P_1\text{-}1s^2$	7.40159(0.6)	7.40206(20)	7.40220(14)	7.40086(11)				7.40196(14)	7.40270(10)
$4\times 1s2p\ ^3P_1\text{-}1s^2$	7.43806(0.6)	7.43821(21)	7.43908(16)	7.43658(6)				7.43886(15)	7.43891(11)
$3\times 1s2p\,^1P_1\text{-}1s^2$	5.55120(0.5)			5.54987(37)	5.54964(33)	5.55076(20)	5.55050(31)		
$3\times 1s2p\ ^3P_1\text{-}1s^{2}$[c]	5.57855(0.5)			5.57232(94)	5.57644(28)	5.57791(56)	5.57709(41)		
$4\times B$	7.48680(374)	7.48443(80)						7.48190(55)	7.48256(9)
$3\times B$	5.61510(281)			5.65446(114)	5.61667(114)				
A	7.49103/222								7.49192(17)
5Lyβ	7.51175(.1)	7.50992(37)		7.50925(47)					7.51204(28)
$1s2p\ ^3P_1\text{-}1s4d\ ^3D_2$	7.61674(80)								7.61705(12)
$1s2p\ ^3P_2\text{-}1s4d\ ^3D_{3+1}$	7.68639(80)								7.68445(19)

[a] Theory is in Å; experiment is in Å; stationary source lines in A317A at 7.45438(226) Å and BX11A at 7.59279(118) Å interfere with the above fits.

[b] $1s5d\ ^3D_{2,1}\text{-}1s2p\ ^3P_1$.

[c] +4Lyδ; $U: 4\times 1s4p-1s^2$? (poor agreement); B: $1s2p^2\ ^4P_{1/2,5/2}\text{-}1s^22p\ ^2P_{1/2,3/2}$; A: $1s4p\ ^3P_{2-0}\text{-}1s2s\ ^3S_1$.

TABLE IX. Heliumlike fine structure $1s2p\ ^3P_1$-$1s^2$ versus $1s2p\ ^1P_1$-$1s^2$, cm^{-1}.

Film	$1s2p\ ^1P_1$-$1s^2$	$1s2p\ ^3P_1$-$1s^2$	Fine structure
A322S	54039012(1460)	53776380(1520)	262632(2106)
B422S	54037988(1022)	53770088(1156)	267900(1543)
A317A	54047772(803)	53788168(434)	262632(913)
A120T	54039736(1022)	53771680(1084)	268056(1490)
BX11A	54034340(730)	53771320(795)	263020(1079)
A317A, third order	54055320(3604)	53837541(9082)	217779(9771)
A120M, third order	54057560(3214)	53797763(2701)	259797(4198)
B220B, third order	54046653(1947)	53783586(5400)	263067(5740)
A320A, third order	54049185(3019)	53791493(3954)	257691(4975)
Mean, third order			256711(11320)
Mean, fourth order			264213(2331)
Estimate of systematics			±382
Theory [63]	54042444(44)	53777464(44)	264980(64)
Theory [64]	54040100(5404)	53777000(5378)	263100(5400)

interval of fluorine at the 22 ppm [52,53] or 32 ppm [54–56] level, of very high accuracy, but disagreed with theory by 30 σ. Conversely, the agreement of the current result with theory is $\frac{1}{50}$ of the current quoted uncertainty. In lower Z regimes, good success has been observed for laser resonance experiments [57].

$2s$-$2p$ Lamb shift measurements at the 1% level in argon, at the 0.2% level in sulfur, and at the 25 ppm level in helium are sensitive to $2p$ QED at the 36%, 7%, and 0.2% levels [58–60] but do not observe $2p$ fine-structure intervals, so may be dominated by corresponding $2s$ shifts. Comparisons of $2p_{1/2}$ to $2p_{3/2}$ have been made for hydrogen and helium to high precision [61], but the scaling of higher-order terms may lead to important tests at medium Z. The current 0.1% f.s. precision result gives a critical $2p_{3/2}$-$2p_{1/2}$ fine-structure measurement above $Z=2$ sensitive to the corresponding Lamb shift contribution (at the 50% level).

XI. SECONDARY FEW-ELECTRON WAVELENGTHS AND FINE-STRUCTURE MEASUREMENTS

Secondary peak locations have just been used to limit possible systematics, but they may also be used to measure wavelengths of secondary peaks, especially where theoretical uncertainty is significant. Accuracy is limited by uncertainty in source and diffraction corrections, and for weak peaks by statistical uncertainty, but for few-electron systems this can allow improvement over theory.

Results from global fits analogous to Table V are summarized in Tables VIII and IX. The local hydrogenic spectrum is fitted to the (global) dispersion model. Tabulated uncertainties here refer to statistical scatter only.

Theory quoted is that of Drake [62,63] for $1snl$ states up to $n=3$, with corrected values from [64] for $n=4-5$. Lithiumlike wavelengths are taken from [64,65].

Fourth-order resonance lines are in good agreement with theory, with third-order values being slightly low. Several third-order peaks are approximately 100 ppm low, corresponding to source corrections for in-target excitation. This should be less important for first-order lines, as seen for the $1s4p$-$1s2s$ transition. $1s5l$-$1s2s$ transitions appear to show a $100-200$ ppm reduction from theory, which could be due to theory, statistics, and excitation location.

Agreement with identified lines is very good, except for the line labeled U, which was only observed in ADP diffraction, on the long-wavelength side of Balmer δ. It is several times stronger than the latter, and also appears to lie on the long-wavelength side of the $1s4p$-$1s^2$ transitions. This discrepancy could be a multielectron peak or contaminant, and some correction might be needed for diffraction and source corrections, especially near the end of the image range.

Lyman β in fifth order is observed and interferes with nearby heliumlike and lithiumlike peaks. Linearization of fifth-order peaks is generally based on fourth-order energies, but centroids should be accurate. A peak due to $1s2p^2\ ^2D_{5/2}$-$1s^22p\ ^2P_{3/2}$ at 1.8654 Å nearly overlaps Balmer η and $1s2p$-$1s^2$. Theoretical uncertainty for this and first-order lines is quite large, and results therefore provide a test of calculation methods (and theory).

The resonance lines in third and fourth order provide differential measurements of the $1s2p$ fine structure, which again avoid much of the uncertainty of the dispersion calibration. This is presented in Table IX. Third-order measurements are given for completeness, but are shifted to shorter wavelengths by Lyman δ, particularly for ADP diffraction, so are neglected in the overall mean. BX11A gives poor absolute measurements and can involve significant crystal effects, but is able to provide a reasonable measurement here with high precision. Diffraction effects are included to first order, and the systematic uncertainty for the shifts discussed above is approximately 50 ppm of the transitions, as noted. The accuracy is limited by statistics. However, this accuracy lies at the same level of precision for other heliumlike measurements in this range of Z [45].

XII. SUMMARY AND CONCLUSION

This was a long and complex experiment, collecting a large group of data sets of high-resolution x-ray emulsion using curved-crystal diffraction. Neither crystal defects nor photographic linearization were significant limitations of the accuracy, and in general, the statistics were excellent. However, this did require careful evaluation of photographic theory [66–68].

A key failure of many prior analyses was the neglect of systematic diffraction shifts especially between different orders of diffraction. This work has reduced this uncertainty to a low level. Nonetheless, care must be taken to properly assess any calibration of one diffraction order by another [29,30,69]. Equally, dynamical diffraction theory depends upon accurate atomic form factors, especially for profile asymmetries [70–72].

This work depended upon in-beam calibration lines. At an accelerator facility this (Lyman α–Balmer β) approach automatically cancels several effects relating to Doppler shifts. We note that secondary cancellations were also necessary, including the use of paired Johann circles on opposite sides of the beam, and using two-dimensional detection to quantify the slope of the image.

One of the great achievements of this experimental setup was the simultaneous measurement of much of the Lyman and Balmer series, so that high-resolution data could be obtained for ranges of energy usually only accessible with low-resolution solid-state detectors. This spectral range permitted calibration of the dispersion of the crystal spectrometer to very high accuracy, beyond the Lyman α–Balmer β intercomparison technique. This also permitted an extensive analysis of the population mechanisms in a beam-foil environment.

We have assessed contributions of dielectronic satellites, Lyman γ, $2s$-$1s$, and $4f$-$2p$ components, which have generally been neglected in earlier analyses. We find that their contributions are small compared to the statistical precision, the dynamical diffraction theoretical uncertainty for this experiment, and the fitting errors. We have considered limits to the final results based on profile widths, model analysis, Yrast limits, and Lyman β spectra, and find that each method yields a consistent result. Our final result is based upon the Lyman β analysis, which has a relatively low uncertainty.

Hence we obtain a measurement of the Lamb shift for hydrogenic iron *for the Lyman α transitions* as provided in Table VI. For Lyman α_1, the Lamb shift is measured to be 35 376 cm^{-1} with a statistical uncertainty (one standard deviation) of 641 cm^{-1} and a systematic uncertainty of 1817 cm^{-1}. Similarly, the Lamb shift for Lyman α_2 is measured to be 35 953 cm^{-1} with a statistical uncertainty (one standard deviation) of 432 cm^{-1} and a systematic uncertainty of 1766 cm^{-1}. This represents a 5.7% measurement of the hydrogenic $1s$-$2p_{1/2}$ Lamb shift in iron.

The two-sigma (standard deviation) discrepancy from theory could possibly relate to dominant uncertainties from Yrast contributions, initial populations, and decay locations in the observation region. However, the result compares well with past measurements in this region of Z. The key problem relates to the Doppler shift arising from differences in the source location. Even with a 1 mm or 2 mm observation length this remains the dominant limitation of this particular experiment.

A difficulty of this particular experiment is the care needed with densitometry and photographic theory, whereas electronic real-time data collection can offer significant simplification of analysis. However, either type of experiment at an accelerator environment will be limited by the accuracy of the downstream decay location of any in-beam sources, or equivalently by the calibration of Doppler velocities. This can be addressed by narrower slits and additional information from careful population mechanics, in part from solid-state spectra, so that these experiments can certainly reach statistical accuracies below 1–4 ppm and systematic uncertainties below 15–20 ppm. Where an ultimate limit would be, would be too speculative, but key goals of investigating higher-order and excited-state QED contributions are certainly achievable across the medium-Z range of the periodic table.

Importantly, most dominant uncertainties cancel when the same data is analyzed to measure the hydrogenic $2p_{3/2}$-$2p_{1/2}$ fine structure to be 171 108 $\text{cm}^{-1} \pm 180\ \text{cm}^{-1}$. This then represents a discrepancy from theory [24] of only 4 $\text{cm}^{-1} \pm 180\ \text{cm}^{-1}$, which compares to the best quoted previous measurement of $-904\ \text{cm}^{-1} \pm 1600\ \text{cm}^{-1}$ [35]. As opposed to some prior measurements, we measure both Lyman α components and can extract a fine-structure measurement directly using the same calibrated dispersion axis. This result is in excellent agreement with theory, the discrepancy of 1% of the Lamb shift contribution to the Lyman α fine structure being quite dominated by the 51% uncertainty. Finally, we report measurements of secondary lines, especially including the heliumlike iron fine structure for $1s2p\ {}^3P_1$-$1s^2$ versus $1s2p\ {}^1P_1$-$1s^2$, cm^{-1}.

---

[1] W. E. Lamb and R. C. Retherford, Phys. Rev. **79**, 549 (1950).

[2] M. Niering, R. Holzwarth, J. Reichert, P. Pokasov, T. Udem, M. Weitz, T. W. Hansch, P. Lemonde, G. Santarelli, M. Abgrall, P. Laurent, C. Salomon, and A. Clairon, Phys. Rev. Lett. **84**, 5496 (2000).

[3] S. G. Karshenboim and V. B. Smirnov, in *Precision Physics of Simple Atomic Systems*, edited by S. G. Karshenboim and V. B. Smirnov, Lecture Notes in Physics (Springer, New York, 2003), pp. 1–10.

[4] S. J. Brodsky and P. J. Mohr, in *Structure and Collisions of Ions and Atoms*, edited by I. A. Sellin (Springer-Verlag, Berlin, 1978), pp. 3–67.

[5] P. J. Mohr and B. N. Taylor, Rev. Mod. Phys. **72**, 351 (2000).

[6] G. W. F. Drake, W. Nortershauser, and Z.-C. Yan, Can. J. Phys. **83**, 311 (2005).

[7] P. H. Mokler, Radiat. Phys. Chem. **75**, 1730 (2006).

[8] R. Reuschl, A. Gumberidze, T. Stohlker, C. Kozhuharov, J. Rzadkiewicz, U. Spillman, S. Tashenov, S. Fritzsche, and A. Surzhykov, Radiat. Phys. Chem. **75**, 1740 (2006).

[9] J. D. Silver, A. F. McClelland, J. M. Laming, S. D. Rosner, G. C. Chandler, D. D. Dietrich, and P. O. Egan, Phys. Rev. A **36**, 1515 (1987).

[10] C. T. Chantler, D. Paterson, L. T. Hudson, F. G. Serpa, J. D. Gillaspy, and E. Takacs, Phys. Rev. A **62**, 042501 (2000).

[11] S. B. Utter, P. Beiersdorfer, and G. V. Brown, Phys. Rev. A **61**, 030503(R) (2000).

[12] S. G. Karshenboim, Phys. Rep. **422**, 1 (2005).

[13] U. D. Jentschura and J. Evers, Can. J. Phys. **83**, 375 (2005).

[14] P. J. Mohr, in *Physics of Highly-Ionized Atoms*, edited by R. Marrus, NATO Advanced Studies Institute Series B: Physics (Plenum, New York, 1989), Vol. 201, pp. 111–141.

[15] M. N. Kinnane, J. A. Kimpton, and C. T. Chantler, Radiat. Phys. Chem. **75**, 1744 (2006).

[16] C. J. Hailey, R. E. Stewart, G. A. Chandler, D. D. Dietrich, and R. J. Fortner, J. Phys. B **18**, 1443 (1985).

[17] D. D. Dietrich, G. A. Chandler, R. J. Fortner, C. J. Hailey, and R. E. Stewart, Phys. Rev. Lett. **54**, 1008 (1985).

[18] J. M. Laming, C. T. Chantler, J. D. Silver, D. D. Dietrich, E. C. Finch, P. H. Mokler, and S. D. Rosner, Nucl. Instrum. Methods Phys. Res. B **31**, 21 (1988).

[19] C. T. Chantler, Can. J. Phys. (to be published).

[20] C. T. Chantler, D.Phil. thesis, Oxford, 1990.

[21] V. I. Kushnir, J. P. Quintana, and P. Georgopoulos, Nucl. Instrum. Methods Phys. Res. A **328**, 588 (1993).

[22] A. J. Varney, D.Phil. thesis, Oxford, 1995.

[23] P. J. Mohr, At. Data Nucl. Data Tables **29**, 453 (1983).

[24] W. R. Johnson and G. Soff, At. Data Nucl. Data Tables **33**, 405 (1985).

[25] G. W. Erickson, J. Phys. Chem. Ref. Data **6**, 831 (1977).

[26] S. Klarsfeld and A. Maquet, Phys. Lett. **43B**, 201 (1973).

[27] G. W. F. Drake, Can. J. Phys. **66**, 586 (1988).

[28] L. A. Vainshtein and U. I. Safranova, Phys. Scr. **31**, 519 (1985).

[29] C. T. Chantler, J. Appl. Crystallogr. **25**, 674 (1992).

[30] C. T. Chantler, J. Appl. Crystallogr. **25**, 694 (1992).

[31] J.-P. Briand, M. Tavernier, P. Indelicato, R. Marrus, and H. Gould, Phys. Rev. Lett. **50**, 832 (1983).

[32] J. M. Laming, D.Phil. thesis, Oxford, 1988.

[33] A. F. McClelland, D.Phil. thesis, Oxford, 1989.

[34] J.-P. Briand, J. P. Mosse, P. Indelicato, P. Chevallier, D. Girard-Vernhet, A. Chetioui, M. T. Ramos, and J. P. Desclaux, Phys. Rev. A **28**, 1413 (1983).

[35] J.-P. Briand, M. Tavernier, R. Marrus, and J. P. Desclaux, Phys. Rev. A **29**, 3143 (1984).

[36] E. Källne, J. Källne, P. Richard, and M. Stöckli, J. Phys. B **17**, L115 (1984).

[37] R. D. Deslattes, R. Schuch, and E. Justiniano, Phys. Rev. A **32**, 1911 (1985).

[38] M. R. Tarbutt and J. D. Silver, J. Phys. B **35**, 1467 (2002).

[39] L. Schleinkofer, F. Bell, H.-D. Betz, G. Trollmann, and J. Rothermel, Phys. Scr. **25**, 917 (1982).

[40] H. Gould and C. T. Munger, *Atomic Physics*, edited by H. Narumi, and I. Shimamura (Elsevier, Amsterdam, 1987), Vol. 10, pp. 77–93.

[41] J. P. Buchet, M. C. Buchet-Poulizac, A. Denis, J. Desesquelles, M. Druetta, J. P. Grandin, and X. Husson, Phys. Rev. A **23**, 3354 (1981).

[42] R. DeSerio, H. G. Berry, R. L. Brooks, J. Hardis, A. E. Livingston, and S. J. Hinterlong, Phys. Rev. A **24**, 1872 (1981).

[43] T. J. Scholl, R. A. Holt, and S. D. Rosner, Phys. Rev. A **39**, 1163 (1989).

[44] P. Zhao, J. R. Lawall, A. W. Kam, M. D. Lindsay, F. M. Pipkin, and W. Lichten, Phys. Rev. Lett. **63**, 1593 (1989).

[45] W. A. Hallett, D.Phil. thesis, Oxford, 1991.

[46] M. N. Kinnane, J. A. Kimpton, M. D. de Jonge, K. Makonyi, and C. T. Chantler, Meas. Sci. Technol. **16**, 2280 (2005).

[47] J. A. Kimpton, M. N. Kinnane, and C. T. Chantler, Rev. Sci. Instrum. **77**, 083102 (2006).

[48] C. T. Chantler, D. Paterson, L. T. Hudson, F. G. Serpa, J. D. Gillaspy, and E. Takacs, Phys. Scr., T **T80B**, 440 (1999).

[49] C. T. Chantler, M. N. Kinnane, C. H. Su, and J. A. Kimpton, Phys. Rev. A **73**, 012508 (2006).

[50] M. N. Kinnane, J. A. Kimpton, and C. T. Chantler, Radiat. Phys. Chem. **75**, 1744 (2006).

[51] C. T. Chantler, Radiat. Phys. Chem. **71**, 611 (2004).

[52] E. G. Myers, D.Phil. thesis, Oxford, 1981.

[53] E. G. Myers, Nucl. Instrum. Methods Phys. Res. B **9**, 662 (1985).

[54] E. G. Myers, P. Kuske, H. J. Andra, I. A. Armour, N. A. Jelley, H. A. Klein, J. D. Silver, and E. Trabert, Phys. Rev. Lett. **47**, 87 (1981).

[55] E. G. Myers, J. K. Thompson, H. S. Margolis, J. D. Silver, and M. R. Tarbutt, Hyperfine Interact. **127**, 323 (2000).

[56] H. J. Andra, Nucl. Instrum. Methods Phys. Res. **202**, 123 (1982).

[57] K. Hosaka, D. N. Crosby, K. Gaarde-Widdowson, C. J. Smith, J. D. Silver, T. Kinugawa, S. Ohtani, and E. G. Myers, Phys. Rev. A **69**, 011802 (2004).

[58] H. Gould and R. Marrus, Phys. Rev. A **28**, 2001 (1983).

[59] A. P. Georgiadis, D. Muller, H. D. Strater, J. Gassen, P. Vonbrentano, J. C. Sens, and A. Pape, Phys. Lett. A **115**, 108 (1986).

[60] G. W. F. Drake, J. Patel, and A. van Wijngaarden, Phys. Rev. Lett. **60**, 1002 (1988).

[61] V. W. Hughes, *Atomic Physics*, edited by H. Narumi and I. Shimamura (Elsevier, Amsterdam, 1987), Vol. 10, pp. 1–34.

[62] G. W. F. Drake (unpublished).

[63] G. W. F. Drake, Can. J. Phys. **66**, 586 (1988).

[64] L. A. Vainshtein and U. I. Safranova, Phys. Scr. **31**, 519 (1985).

[65] L. A. Vainshtein and U. I. Safranova, At. Data Nucl. Data Tables **21**, 49 (1978).

[66] C. T. Chantler, Appl. Opt. **32**, 2371 (1993).

[67] C. T. Chantler, Appl. Opt. **32**, 2398 (1993).

[68] C. T. Chantler, J. D. Silver, and D. D. Dietrich, Appl. Opt. **32**, 2411 (1993).

[69] C. T. Chantler and R. D. Deslattes, Rev. Sci. Instrum. **66**, 5123 (1995).

[70] C. T. Chantler, Radiat. Phys. Chem. **41**, 759 (1993).

[71] C. T. Chantler, in *Resonant Anomalous X-Ray Scattering. Theory and Applications*, edited by G. Materlik, K. Fischer, and C. J. Sparks (Elsevier, North-Holland, 1994).

[72] C. T. Chantler, J. Phys. Chem. Ref. Data **24**, 71 (1995); C. T. Chantler, *ibid.* **29**, 597 (2000).